A&A 492, 743–755 (2008)
DOI: 10.1051/0004-6361:200810525

Astronomy & Astrophysics

A CO $J = 1$–0 survey of common optical/*uv* absorption sightlines*

H. S. Liszt

National Radio Astronomy Observatory, 520 Edgemont Road, Charlottesville, VA, 22903-2475, USA
e-mail: `hliszt@nrao.edu`

Received 4 July 2008 / Accepted 17 October 2008

ABSTRACT

Context. Comparison of optical/uv absorption line data with high-resolution profiles of mm-wave CO emission provides complementary information on the absorbing gas, as toward ζ Oph. Over the past thirty years a wealth of observations of CO and other molecules in optical/uv absorption in diffuse clouds has accumulated for which no comparable CO emission line data exist.
Aims. To acquire mm-wave $J = 1$–0 CO emission line profiles toward a substantial sample of commonly-studied optical/uv absorption line targets and to compare with the properties of the absorbing gas, especially the predicted emission line strengths.
Methods. Using the ARO 12 m telescope, we observed mm-wavelength $J = 1$–0 CO emission with spectral resolution $R \approx 3 \times 10^6$ and spatial resolution 1′ toward a sample of 110 lines of sight previously studied in optical/uv absorption lines of CO, H_2, CH, etc.
Results. Interstellar CO emission was detected along 65 of the 110 lines of sight surveyed and there is a general superabundance of CO emission given the distribution of galactic latitudes in the survey sample. Much of the emission is optically thick or very intense and must emanate from dark clouds or warm dense gas near HII regions.
Conclusions. Judging from the statistical superabundance of CO emission, seen also in the total line of sight reddening, the OB star optical/*uv* absorption line targets must be physically associated with the large quantities of neutral gas whose CO emission was detected, in which case they are probably influencing the absorbing gas by heating and/or photoionizing it. This explains why CO/H_2 and ^{12}CO/^{13}CO ratios differ somewhat between *uv* and mm-wave absorption line studies. Because the lines of sight have been preselected to have $A_V \lesssim 1$ mag, relatively little of the associated material actually occults the targets, making it difficult for CO emission line observations to isolate the foreground gas contribution.

Key words. ISM: molecules – ISM: clouds – astrochemistry

1. Introduction

The presence of gas-phase carbon monoxide (CO) in diffuse clouds at $A_V \lesssim 1$ mag was shown by Smith & Stecher (1971) shortly after the discovery of interstellar CO itself via the intense mm-wave CO $J = 1$–0 rotational emission in the Orion Nebula (Wilson et al. 1970). Although the fractional abundance of CO is relatively small in diffuse clouds, typically $10^{-7} < N(\mathrm{CO})/N(\mathrm{H_2}) < 10^{-5}$ so that $N(\mathrm{CO}) \ll N(\mathrm{C^+})$ and at most a few percent of the free gas-phase carbon is actually in CO, the presence of even this much CO has proved a consistent challenge to interstellar chemistry (Glassgold & Langer 1976; Black & Dalgarno 1977; Bally & Langer 1982; Glassgold et al. 1985; Van Dishoeck & Black 1988; Lee et al. 1996).

It is only quite recently that substantial numbers of sightlines have been studied with high sensitivity in *uv* absorption with HST and FUSE (Sonnentrucker et al. 2007; Burgh et al. 2007; Sheffer et al. 2007, 2008) and in mm-wave absorption against extragalactic continuum sources (Liszt & Lucas 1998) at the PdBI so that the formation, excitation and fractionation of CO in diffuse clouds can be considered in a systematic fashion (ibid and Liszt 2007); compare with the much earlier survey of Federman et al. (1980). Notwithstanding the long interval since its discovery, carbon monoxide is now the molecule whose chemistry and abundance relative to H_2 are the most exhaustively studied in the diffuse interstellar medium (ISM). With much scatter, $N(\mathrm{CO}) \propto N(\mathrm{H_2})^2$ for 10^{12} cm^{-2} $<$ $N(\mathrm{CO})$ 3×10^{16} cm^{-2}, $10^{19} < N(\mathrm{H_2}) \lesssim 2 \times 10^{21}$ cm^{-2}.

From the CO column densities and rotational excitation temperatures observed in absorption, it is straightforward to calculate that the integrated brightness temperature of CO $J = 1$–0 rotational emission in diffuse gas should vary as $W_{\mathrm{CO}} = \int T_{\mathrm{B}} \mathrm{d}v \approx 1$ K km s^{-1} $\times N(\mathrm{CO})/10^{15}$ cm^{-2} for $N(\mathrm{CO}) \lesssim 10^{16}$ cm^{-2} and W_{CO} as strong as 10–12 K km s^{-1} (Liszt 2007). This was actually observed when comparing CO emission and absorption at mm-wavelengths toward distant extragalactic background sources, where separating foreground and background gas is not an issue (Liszt & Lucas 1998). It is also correct along the archetypal line of sight toward ζ Oph at $N(\mathrm{CO}) = 2.2 \times 10^{15}$ cm^{-2}. Proportionality between W_{CO} and $N(\mathrm{CO})$ is a very general consequence of weak excitation, i.e. $T_{\mathrm{ex}} \ll T_{\mathrm{K}}$ (Goldreich & Kwan 1974) but the normalization is determined by ambient physical conditions. As discussed below (see Sect. 5), $W_{\mathrm{CO}}/N(\mathrm{CO})$ is about 50 times higher in diffuse clouds than toward Orion A or typical dark clouds.

The CO emission from absorbing foreground material in diffuse clouds should be readily detectable if $N(\mathrm{CO}) \gtrsim 3 \times 10^{14}$ cm^{-2} and rather strong, comparable to the emission from dark clouds, whenever $N(\mathrm{CO}) \gtrsim 10^{15}$ cm^{-2}. Morever, if CO emission is observable, the high spectral resolution available in mm-wave spectra, typically $R \approx 3 \times 10^6$, provides complementary information to that available in lower-resolution absorption spectra (Knapp & Jura 1976; Liszt 1979; Wannier et al. 1982; Langer et al. 1987; Wilson et al. 1992; Nehmé et al. 2008). As well, the identification of absorbing gas in CO emission would

---

* Based on observations obtained with the ARO Kitt Peak 12 m telescope.

offer the prospect of relatively high spatial resolution imaging of the absorption line host body. This being the case, it seemed reasonable to survey CO J = 1–0 rotational emission toward a substantial sample of commonly-observed optical/*uv* absorption sightlines. A small but nominally similar survey was performed at a much earlier epoch by Knapp & Jura (1976), with somewhat mixed results owing to confusion between telluric and interstellar emission (Appendix A). The results are somewhat mixed here as well owing to confusion between telluric and interstellar emission (Appendix A). The results are somewhat mixed here as well owing to confusion between foreground and background material (see Nehmé et al. 2008), combined with the propensity for early-type absorption line target stars to be associated with but in front of large amounts of neutral material as discussed in Sects. 4 and 5.

Section 2 here describes the data which were taken to implement the survey and the methods of sightline selection, data reduction and presentation. Section 3 describes the observational results. Section 4 reports the survey statistics and discusses some evident biases. Section 5 discusses the apparent difficulties in separating foreground and background gas in emission and Sect. 6 is a summary. Appendices A–C discuss various observational aspects of the implementation of the present survey, including telluric CO emission, spectral baseline removal and deconvolution of frequency-switching (respectively) .

2. Sample selection and overlap with prior work

The goal of this work was to observe as many targets as possible given prior absorption line surveys of important species H_2, CO, OH, CH, CH^+ and $H_3{}^+$. Owing to terrestrial geography, only targets above –25° declination were included; given that absorption lines of H_2 and CO are observed from space and that that the center of the Galaxy is in the southern sky, this criterion eliminated many sightlines. The final target list numbered 110 and two sightlines near Orion B were added to the observational program (but excluded from calculation of the statistics) as controlled examples of heated gas along sightlines to well-studied HII regions (Pety et al. 2007).

First priority was given to sightlines observed in *uv* CO absorption by Sonnentrucker et al. (2007), Burgh et al. (2007) and Sheffer et al. (2007). These references also tabulate or provide values or new measurements of $N(H_2)$. Sightlines having measured $N(H_2)$ not included in the CO surveys were taken from the work of Savage et al. (1977) and Rachford et al. (2002). CH column densities for sources surveyed in CO absorption are included in the work of Sonnentrucker et al. (2007) and some further sightlines studied in CH were taken from the work of Crane et al. (1995)[1]. Finally, a few sightlines were included which have recently between observed in CH^+ by (Stahl et al. 2008, CH^+ was also surveyed by Crane et al. 1995) and in $H_3{}^+$ absorption by McCall et al. (2002).

3. Observations and data reduction

The new data discussed here, profiles of J = 1–0 ^{12}CO and ^{13}CO emission, were acquired at the ARO 12 m telescope during 2007 December and to a lesser extent in 2008 January and February, to make up for time lost to weather and objects too close to the Sun earlier. The observations are somewhat time-specific because of the presence of telluric emission in the ^{12}CO spectra. At the frequency of the ^{12}CO J = 1–0 line, 115.3 GHz, the half-power beamwidth of the 12 m antenna is 65″. Line brightnesses from the 12 m telescope are on a T_r^* scale and should be scaled upward by a factor 0.85/0.72 = 1.2 to derive corresponding main-beam brightness.

In an all-sky survey of this sort it is not practicable to search for nearby off-source positions which are free of emission at low levels. Therefore, the raw data were taken in a frequency-switching mode (Liszt 1997) with the 6144-channel mm-wave autocorrelator (MAC) at 24.4 kHz resolution (0.0635 km s^{-1} at the ^{12}CO rest frequency). The throw of the frequency-switch was ±1 MHz for most spectra and ±2 MHz for a few others which at ±1 MHz were hard to reconstruct faithfully. Typical integration times were 12–18 min in each of two polarizations resulting in a typical rms of 0.1 K after the spectra were co-added in the two polarizations and hanning-smoothed to a final resolution of 48.8 kHz (0.127 km s^{-1} for ^{12}CO).

The baselines in frequency-switched data at some mm-wave telescopes are bad enough to prevent reliable reconstruction (unfolding) of broad-band spectra, but those at the 12 m were sums of two or three pure sine-waves, typically dominated by periods of approximately 156 and 17.4 MHz (400 and 35 km s^{-1}, respectively for ^{12}CO), making baseline subtraction simple. This is illustrated in Appendix B and Fig. A.2.

The data were unfolded using the EKHL algorithm (Liszt 1997) illustrated in Fig. A.3 and discussed in Appendix C. This technique, analogous to the dual-beam switching procedure for spatial mapping, allows recovery of spectra with frequency-switch intervals smaller than the extent of the emission profile, as long as the spectral baselines are flat. In turn, because the switching interval may be made smaller, the baselines may also improve. There is a penalty to be paid in terms of time because the rms noise may not decrease much after unfolding, but this is negligible compared to the amount of time which would be spent hunting for a suitable off-source reference position (which would be followed by observing in a position-switching mode, with less than half the observing time spent on-source anyway). The penalty is also negligible compared to the process detailed in Fig. 8 of McCall et al. (2002) where spectra taken with 3 frequency throws toward HD 183143 did not yield a spectrum showing all the emission present along the line of sight (see Fig. 2 here).

The velocity scale of all the spectra is with respect to the LSR. The data output from the 12 m are on a T_r^* scale, that is, corrected for a beam efficiency of 0.85 corresponding to the forward response falling within the area of the Moon. To put the interstellar data on a main-beam scale, the spectra should be scaled up by a factor ≈1.2 (0.85/0.7) corresponding to the full main beam efficiency.

The survey results are summarized in Tables 1–4. Table 1 describes sightlines lacking detected interstellar emission; it provides the galactic coordinates, the (date-specific) mean lsr velocity at which telluric emission appeared in the spectra (labelled $v_{\rm tel}$), the channel to channel rms of the reduced, coadded and smoothed ARO spectrum and the log of the absorbing CO and H_2 column densities known from other work. Tables 2 and 3 summarize the lines of sight with detected interstellar CO. For each source they provide galactic coordinates, the reddening out to infinity from the work of Schlegel et al. (1998), the foreground reddening copied from earlier references, $v_{\rm tel}$, followed by the peak and integrated T_r^*, the mean velocity of the emission (which in a few cases contains an indistinguishable telluric

---

[1] Several of the lines of sight in the work of Crane et al. (1995) are denoted by their HR numbers, specifically HR 1156 = HD 23480, HR 1178 = HD 23850, HR 2135 = HD 41117 and HR 6812 = HD 166937.

Table 1. Sightlines lacking interstellar CO $J = 1$–0 emission[1].

Target HD	l °	b °	$v_{\rm tel}$ km s^{-1}	rms K	N(CO) cm^{-2}	N(H$_2$) cm^{-2}
13994	134.39	–3.42	–6.17	0.098		
21856	196.46	–50.96	–29.36	0.124		20.04
22951	158.92	–16.70	–14.08	0.087	14.22	20.46
23408	166.17	–23.51	–18.11	0.098		19.75
23480	166.57	–23.75	–17.98	0.169		20.12
23630	166.67	–23.46	–18.32	0.088	<12.34	19.54
23850	167.01	–23.23	–18.56	0.162		
23840	159.46	–15.03	–33.41	0.055		
24912	160.37	–13.11	–12.78	0.066	13.49	20.53
30614	144.07	14.04	–14.38	0.073	14.49	20.34
34078	172.08	–2.26	–6.72	0.126		
35149	199.16	–17.86	–14.71	0.107	<13.00	18.30
36486	203.86	–17.74	–14.17	0.116	<12.04	14.74
37128	205.21	–17.24	–14.13	0.085	<12.30	16.28
42087	187.75	1.77	–30.60	0.098		
57060	237.82	–5.37	–5.79	0.157	<12.67	15.78
57061	238.18	–5.54	–5.89	0.158	<12.61	15.48
58510	235.52	–2.47	–23.78	0.138		
121968	333.97	55.84	29.95	0.145	<12.30	18.70
143275	350.10	22.49	18.28	0.099	12.49	19.41
144217	353.19	23.60	35.21	0.116	13.63	19.83
144470	352.75	22.77	34.93	0.120	12.95	20.05
145502	354.61	22.70	34.88	0.120	12.76	19.89
164353	29.73	12.63	10.47	0.086	13.04	20.26
166937	10.00	–1.60	24.39	0.131		
167971	18.25	1.68	5.93	0.129		
170074	75.06	23.71	14.80	0.090		
177989	17.81	–11.88	–1.67	0.123	14.64	20.23
181615	21.84	–13.77	–2.31	0.153		
184915	31.77	–13.29	–2.70	0.101		20.31
192639	74.90	1.48	2.07	0.131	14.13	20.69
193237	75.83	1.32	2.23	0.102		
197592	30.70	–32.15	–13.21	0.121		
198478	85.75	1.49	1.09	0.102		
198781	99.94	12.61	6.23	0.066	15.22	20.56
199579	85.70	–0.30	0.23	0.112		20.36
201345	78.44	–9.54	–4.69	0.064	<12.40	19.43
203064	87.61	–3.84	–1.71	0.092		20.29
206773	99.80	3.62	0.55	0.101	14.20	20.47
209339	104.58	5.87	1.96	0.105	13.95	20.25
209975	104.87	5.39	1.80	0.080		20.08
217035	110.25	2.86	–0.26	0.090	14.57	20.95
217675	102.21	–16.10	–10.33	0.135	12.75	19.67
218915	108.06	–6.89	–5.68	0.134	13.64	20.15
224572	115.55	–6.36	–5.99	0.113		

[1] For explanation of table entries see Sect. 3; all column densities are logarithmic.

contribution), the correction $V_{\rm lsr} - V_{\rm hel}$ which may be subtracted from the lsr velocity scale to convert to heliocentric velocity, followed by the log of the absorption line column densities of CO and H$_2$. Table 4 provides relevant information for the 14 lines of sight where ^{13}CO was also observed. Integration times for these lines of sight were somewhat longer, typically 24 min.

Thumbnail plots of the spectra with detectable interstellar CO emission are shown in Figs. 1–3; where ^{13}CO was observed, those spectra are shown overlaid. When $|v_{\rm tel}| > 10$–15 km s^{-1} and the galactic latitude is a few degrees or more from the galactic plane, overlap with interstellar emission is much less likely. Conversely, there are examples where the telluric line inextricably appears within the velocity range of the interstellar emission and the spectra can only be understood in complete detail with reference to the tabulated telluric velocities $v_{\rm tel}$. In general the telluric and interstellar emission can be separated by observing at several-month intervals.

3.1. Data in machine-readable form

Individual spectra and zip files of all spectra having detected interstellar CO emission are available in CLASS FITS format on NRAO's anonymous ftp server as `http://tinyurl.com/45ps73` and `http://tinyurl.com/5pgju9` for ^{12}CO and ^{13}CO spectra, respectively.

3.2. Detectability of interstellar emission and presentation of upper limits

The spectra acquired here easily detect telluric emission which appears with $W_{\rm CO} \approx 1$ K km s^{-1}/sin (el) and $FWHM = 0.8$ km s^{-1} (see Appendix A); the nominal signal/noise of such a detection is nearly 20:1 for a channel-to-channel rms of 0.1 K. For a 4 km s^{-1} interval, typical of what is needed to bracket a single hypothetical interstellar component, the 3σ rms noise in $W_{\rm CO}$ with single channel rms noise 0.1 K is 0.22 K km s^{-1}. As discussed in Sect. 5 (see Fig. 5 at bottom), interstellar emission was detected in every case, save one, where N(CO) exceeded 4×10^{14} cm^{-2} and emission was expected at a level $W_{\rm CO} > 0.4$ K km s^{-1}. However, both individual components and lines of sight with detected interstellar lines at levels $W_{\rm CO} < 1$ K km s^{-1} are rare. Because no threshold for CO emission is expected empirically ($W_{\rm CO} \propto N$(CO), see Fig. 6 of Liszt 2007), the actual a posteriori sensitivity of the survey may be somewhat poorer than suggested by the detectability of the narrow telluric emission or the 0.1 K single channel rms noise. Where upper limits appear in the Figs. 4 and 5, they are shown symbolically at $W_{\rm CO} < 0.8$ K km s^{-1}. The non-detections in Table 1 should be reliable at a level $W_{\rm CO} < 0.5$–0.8 K km s^{-1}.

4. Survey results

4.1. Statistics and biases

Given that the purpose of the survey (which was achieved) was to provide line profiles toward a pre-defined but rather ad hoc group of target sightlines, the statistical properties of the CO emission found in the survey might not seem to be of much intrinsic value. However, they serve to show that the targets are associated with the gas detected (making the gas atypical of the diffuse ISM as a whole) and that CO emission surveys which seek the foreground gas contribution toward bright stars are heavily contaminated (if not totally corrupted) by material lying behind the absorption targets.

This contamination occurs for several reasons. First is the innate inability of the emission spectra to discriminate between foreground and background placement of material near the target in the absence of other information (for instance, but not necessarily conclusively, the velocity profile of the absorbing gas). Second is the fact that when substantial amounts of gas *are* present along such lines of sight, they will preferentially occur behind the stars, which were a priori selected to observe the diffuse cloud regime $A_{\rm V} \lesssim 1$ mag. Finally, this bias is greatly enhanced by the propensity for the target stars to occur in regions of

Table 2. Sightlines with detected interstellar CO J = 1–0 emission[1].

Target	l °	b °	E_{BV}^{∞} mag	E_{BV} mag	$v_{\rm tel}$ km s^{-1}	rms K	$T_{\rm r}^{*}$ K	$W_{\rm CO}$ K km s^{-1}	$\langle V_{\rm lsr}\rangle$ km s^{-1}	$V_{\rm lsr} - V_{\rm hel}$ km s^{-1}	N(CO) cm^{-2}	N(H$_2$) cm^{-2}
HD 2905	120.84	0.14	1.90	0.01	–2.72	0.179	4.12	8.40	–52.42	7.86		20.27
HD 21483	158.87	–21.30	1.04	0.56	–16.46	0.083	7.59	22.76	6.06	–6.41		
HD23180	160.36	–17.74	4.54	0.30	–14.71	0.108	11.46	19.62	8.51	–6.49	14.83	20.60
HD 281159	160.49	–17.80	10.02	0.85	–14.74	0.059	27.97	41.98	8.35	–6.54		
HD 24398	162.29	–16.69	0.32	0.32	–14.61	0.086	0.97	2.13	8.05	–6.95	14.86	20.67
HD 24534	163.08	–17.14	0.43	0.45	–14.92	0.073	2.55	5.31	7.60	–7.23	16.20	20.92
HD 24760	157.35	–10.09	0.95		–10.71	0.074	4.57	22.68	–5.45	–4.75	11.93	19.52
HD 27778	172.76	–17.39	0.60	0.37	–15.24	0.080	3.38	7.17	5.74	–9.98	16.08	20.79
HD 29647	174.05	–13.35	2.31	1.00	–13.09	0.090	5.84	16.35	6.14	–9.98		
HD 283809	174.16	–13.35	2.33		–13.11	0.114	5.08	16.74	5.95	–10.01		
HD 283879	175.72	–12.61	1.50		–12.71	0.095	6.79	13.23	5.92	–10.36		
HD 36371	175.77	–0.61	1.54	0.43	–6.29	0.137	1.26	3.60	–18.90	–9.04		
HD 36861	195.05	–11.99	0.45	0.12	–11.62	0.119	1.22	1.13	5.12	–14.95	12.59	19.12
HD 37043	209.52	–19.58	1.51	0.07	–15.17	0.106	20.15	58.57	8.01	–17.83	12.43	14.69
HD 37742	206.45	–16.59	4.20	0.08	–13.88	0.096	5.42	18.58	10.06	–17.28	<12.72	15.86
HorseHead	206.96	–16.79	0.98		0.00	0.069	15.92	31.80	9.79	–17.37		
NGC 2024#1	206.53	–16.38	58.85		–37.16	0.064	31.46	156.18	9.95	–17.28		
HD 37903	206.85	–16.54	2.05	0.35	–37.35	0.069	41.20	134.38	9.46	–17.34	14.00	20.92
HD 41117	189.69	–0.86	1.67	0.45	–32.27	0.050	1.75	3.54	4.51	–12.62		
HD 43384	187.99	3.53	0.81	0.58	–29.67	0.114	1.31	1.19	2.41	–11.63		
HD 46202	206.31	–2.00	0.82	0.49	–31.43	0.102	1.38	0.32	9.53	–16.03		
HD46711	208.59	–2.40	2.17	1.04	–31.02	0.103	1.75	2.74	23.23	–16.43		
HD 47129	205.87	–0.31	0.72	0.36	–30.65	0.099	1.35	1.17	20.08	–15.75		20.54
HD 47839	202.94	2.20	6.31	0.07	–3.21	0.090	12.45	47.99	6.87	–14.92	<12.81	15.54
HD 48099	206.21	0.80	1.13	0.27	–30.18	0.095	1.49	1.21	15.98	–15.66		20.29
HD 52382	222.17	–2.15	1.99		–28.05	0.123	2.45	4.86	39.30	–17.94		
HD 53367	223.71	–1.90	6.89	0.74	–27.43	0.109	13.32	47.45	17.22	–18.02		
HD 53974	224.71	–1.79	1.99	0.22	–27.37	0.067	5.29	12.55	15.48	–18.07		
HD 54662	224.17	–0.78	1.61	0.35	–27.21	0.062	4.21	16.63	14.19	–17.91		20.00
HD 147165	351.31	17.00	1.11	0.38	32.57	0.113	2.16	0.46	3.12	9.55	12.48	19.79
HD 147888	353.65	17.71	1.26	0.47	33.10	0.112	3.14	3.49	2.71	10.25	15.30	20.48
HD 147889	352.86	17.04	15.13	1.07	32.76	0.122	16.74	30.86	3.13	9.98		
HD 147933	353.69	17.69	1.23	0.45	32.85	0.124	2.93	3.39	2.63	10.25	15.28	20.57
HD 148184	357.93	20.68	0.49	0.55	34.41	0.105	1.80	1.10	1.14	11.58	14.58	20.63
HD 148605	353.10	15.80	2.03	0.10	32.26	0.123	2.04	0.99	3.67	9.94		18.74

[1] For explanation of table entries see Sect. 3; all column densities are logarithmic.

high gas density, presumably because they are generally of early spectral type and were deemed to be "interesting" for spectroscopic studies.

The association between the targets and the CO emitting gas can be demonstrated in several ways. It is obvious from the spectra that several of the sources (HD 23180, HD 281159, HD 37043, HD 37903, HD 147889) are seen against very strongly-emitting molecular gas characteristic of natal clouds near giant HII regions, while others among the few observed in ^{13}CO show the optically thick CO emission typical of dark clouds (HD 21483, HD 24760, HD 29647, HD 283809). H II regions and dark clouds are rarely found by accident away from the galactic equator. In any case, the strong CO lines indicate very high column densities of material behind which the stars would not be suitable targets for optical/*uv* absorption line studies of diffuse clouds.

The existence of an overendowment of gas along the chosen lines of sight is apparent in at least three ways: the amount of reddening along the ensemble of lines of sight is much higher than expected; CO is detected too frequently and the CO emission is on average too strong. Each of these is discussed separately in the following subsections.

4.2. Reddening and the total gas column

Table 5 gives some statistics of the reddening and integrated CO emission. For a series of minimum separations from the galactic equator $|b|_{<}$ = 3°–20°, the columns of Table 5 show the subsumed number of lines of sight; the number among them with $E_{BV}^{\infty} > 1$ mag; the mean reddening per kpc of equivalent path in the galactic plane $\langle E_{BV}^{\infty}\rangle/\langle l\rangle$, where l = 0.1 kpc/sin (|b|) corresponding to a half-thickness of the dust layer of 100 pc; the number of sightlines with detected CO emission and mean integrated CO emission per unit length (calculated as for the reddening per unit length); the ratio of the reddening and CO emission per unit length, converted to an equivalent column density of H$_2$; and finally, four columns giving the mean foreground and limiting reddening, tabulated separately for sightlines with and without detectable CO emission. To eliminate the influence of a few outliers (see Tables 2, 3), the mean reddening per

Table 3. Sightlines with detected interstellar CO J = 1–0 emission[1].

Target	l °	b °	E_{BV}^{∞} mag	E_{BV}	$v_{\rm tel}$ mag km s^{-1}	rms K	$T_{\rm r}^{*}$ K	$W_{\rm CO}$ K km s^{-1}	$\langle V_{\rm lsr}\rangle$ km s^{-1}	$V_{\rm lsr} - V_{\rm hel}$ km s^{-1}	N(CO) cm^{-2}	N(H$_2$) cm^{-2}
HD 149757	6.28	23.59	0.56	0.32	35.83	0.102	1.60	1.66	–0.07	13.72	15.40	20.64
HD 166734	18.92	3.63	1.52	1.39	7.74	0.094	2.43	3.90	6.15	14.92		
HD 168076	16.94	0.84	25.94	0.78	6.29	0.094	5.99	38.82	0.88	14.19		
HD 168607	14.97	–0.94	8.07	1.61	5.16	0.165	4.77	74.31	38.38	13.55		
HD 169454	17.54	–0.67	13.94	1.12	4.35	0.222	7.72	12.12	5.55	14.12		
HD 172028	31.05	2.83	2.97	0.78	6.45	0.118	7.65	23.03	7.58	16.83		
HD 179406	28.23	–8.31	0.49	0.33	-1.34	0.083	1.26	3.09	2.46	14.82	15.64	20.73
HD 183143	53.24	0.63	3.75	1.27	2.80	0.129	3.03	15.90	–22.61	18.28		
HD 192035	83.33	7.76	0.46	0.28	4.86	0.071	1.16	2.13	5.58	17.10	15.14	20.68
HD 195592	82.36	2.96	2.75	1.18	2.34	0.062	1.14	3.85	2.28	16.74		
CygOB2#8	79.89	0.96	5.83		1.11	0.057	4.95	50.36	–66.24	16.82		
CygOB2#5	80.12	0.91	3.46	1.99	1.33	0.072	2.01	23.26	–3.90	16.79		
CygOB2#12	80.10	0.83	4.18	3.31	0.97	0.063	4.13	27.44	1.93	16.78		
VICYG#8A	80.22	0.79	6.46		1.04	0.062	3.63	27.49	–10.74	16.76		
HD 200120	88.03	0.97	2.67	0.18	0.62	0.061	1.76	9.69	–38.87	15.63	12.18	19.30
HD 203374	100.51	8.62	1.09	0.60	3.89	0.076	1.18	3.19	2.20	14.04	15.41	20.70
HD 203938	90.56	–2.23	1.55	0.74	–1.36	0.073	2.90	4.97	5.15	14.76		
HD 204827	99.17	5.55	1.05	1.11	1.39	0.088	2.81	11.21	–66.86	14.02		
HD 206165	102.27	7.25	0.70	0.47	2.96	0.090	1.27	1.86	–0.36	13.51	15.18	20.78
HD 206267	99.29	3.74	0.98	0.52	1.19	0.084	1.54	2.91	–2.24	13.79	16.04	20.86
HD 207198	103.14	6.99	0.66	0.62	2.67	0.153	1.61	2.63	–26.88	13.29	15.50	20.83
HD 207308	103.11	6.82	0.59	0.50	2.75	0.123	1.88	4.31	–2.18	13.28	15.93	20.86
HD 207538	101.60	4.67	1.19	0.64	1.27	0.082	1.33	2.19	–1.89	13.39	15.40	20.91
HD 208440	104.03	6.44	0.66	0.34	2.28	0.133	1.22	1.10	–1.06	13.02	14.20	20.34
HD 210121	56.88	–44.46	0.22	0.40	–21.62	0.140	2.00	2.91	–6.32	7.76	15.83	20.75
HD 210839	103.83	2.61	1.64	0.56	–0.12	0.107	1.14	4.16	–77.96	12.64	15.44	20.84
HD 216532	109.65	2.68	3.73	0.86	–0.11	0.085	2.35	9.00	–98.72	11.22	15.15	21.10
HD 216898	109.93	2.39	2.86	0.85	–0.66	0.084	0.97	4.59	–9.89	11.11	15.04	21.05
HD 217312	110.56	2.95	1.04	0.66	0.07	0.154	1.60	3.09	–78.91	11.02	14.38	20.80
HD 218376	109.95	–0.78	1.51	0.25	–2.14	0.138	1.47	7.58	–45.05	10.70	14.80	20.15
BD+631964	112.89	3.10	1.70	1.00	–0.05	0.115	1.38	2.73	–10.86	10.43		
HD 229059	75.70	0.40	13.52	1.71	1.05	0.055	10.00	74.64	–52.72	17.24		

[1] For explanation of table entries see Sect. 3; all column densities are logarithmic.

Table 4. Sightlines observed in ^{13}CO[1].

Target HD	rms K	$T_{\rm r}^{*}$ K	W_{13} K km s^{-1}	$\langle V_{\rm lsr}\rangle$ km s^{-1}	W_{12}/W_{13}
21483	0.038	2.23	3.47	5.93	6.56
23180	0.025	0.44	0.84	8.37	23.46
281159	0.033	9.20	13.38	8.61	3.14
24534	0.017	0.22	0.29	7.77	18.49
24760	0.023	1.01	3.02	–4.97	7.52
27778	0.021	0.19	0.43	5.96	16.86
29647	0.031	3.79	5.84	5.88	2.80
283809	0.025	2.27	4.05	5.96	4.13
37043	0.038	4.14	13.92	7.87	4.21
37742	0.030	0.33	0.95	10.10	19.52
47839	0.027	4.98	10.14	7.00	4.73
52382	0.024	0.48	0.63	39.32	7.71
53367	0.047	5.94	13.98	17.41	3.39
53974	0.022	0.29	0.91	16.15	13.82

[1] For explanation of table entries see Sect. 3.

unit length was calculated using sightlines with $E_{BV}^{\infty} < 5$ mag and the mean CO emission per unit length was calculated for $W_{\rm CO} < 50$ K km s^{-1}. The table entries for either quantity would have been 50–75% higher if these limits were not observed.

For a local mean reddening at $z = 0$ of 0.61 mag kpc^{-1} (Spitzer 1978), lines of sight with $E_{BV}^{\infty} > 1$ mag should be confined within about 4° of the galactic plane, which is manifestly not the case here. Moreover, the mean limiting reddening per unit path in Table 5 ranges from 2 to 5 times the local average depending on the lower latitude limit. This can be contrasted with the opposing tendency for absorption line surveys to have smaller than average reddening per unit length when only the foreground material is counted (Savage et al. 1977).

4.3. Frequency of occurence and strength of CO emission

In the present survey, 31 of the 55 lines of sight at $3° < b < 20°$ had detectable emission (56%) compared to 10 of 48 lines of sight (22%) in the same latitude range in a truly blind survey for galactic CO emission toward extragalactic mm-wave radiocontinuum sources (Liszt & Wilson 1993; Liszt 1994). Furthermore, the emission lines found in the blind survey were much weaker, illustrating that the present work also includes a superabundance of integrated CO emission (not just detections) at high latitude. The mean integrated brightnesses per kpc of path in this survey at $|b| > 3°$ are $A_{\rm CO} = 14$–39 K km s^{-1} kpc^{-1}, generally increasing with the lower bound of the latitude range considered. This may be compared with a value $A_{\rm CO} \approx 5$ K km s^{-1} kpc^{-1} at the Solar Circle in surveys of the galactic plane (Burton & Gordon 1978).

4.4. Foreground vs. background reddening

The final four columns of Table 5 give the mean foreground and limiting reddening for sightlines with and without detected CO emission. The sample mean foreground reddening

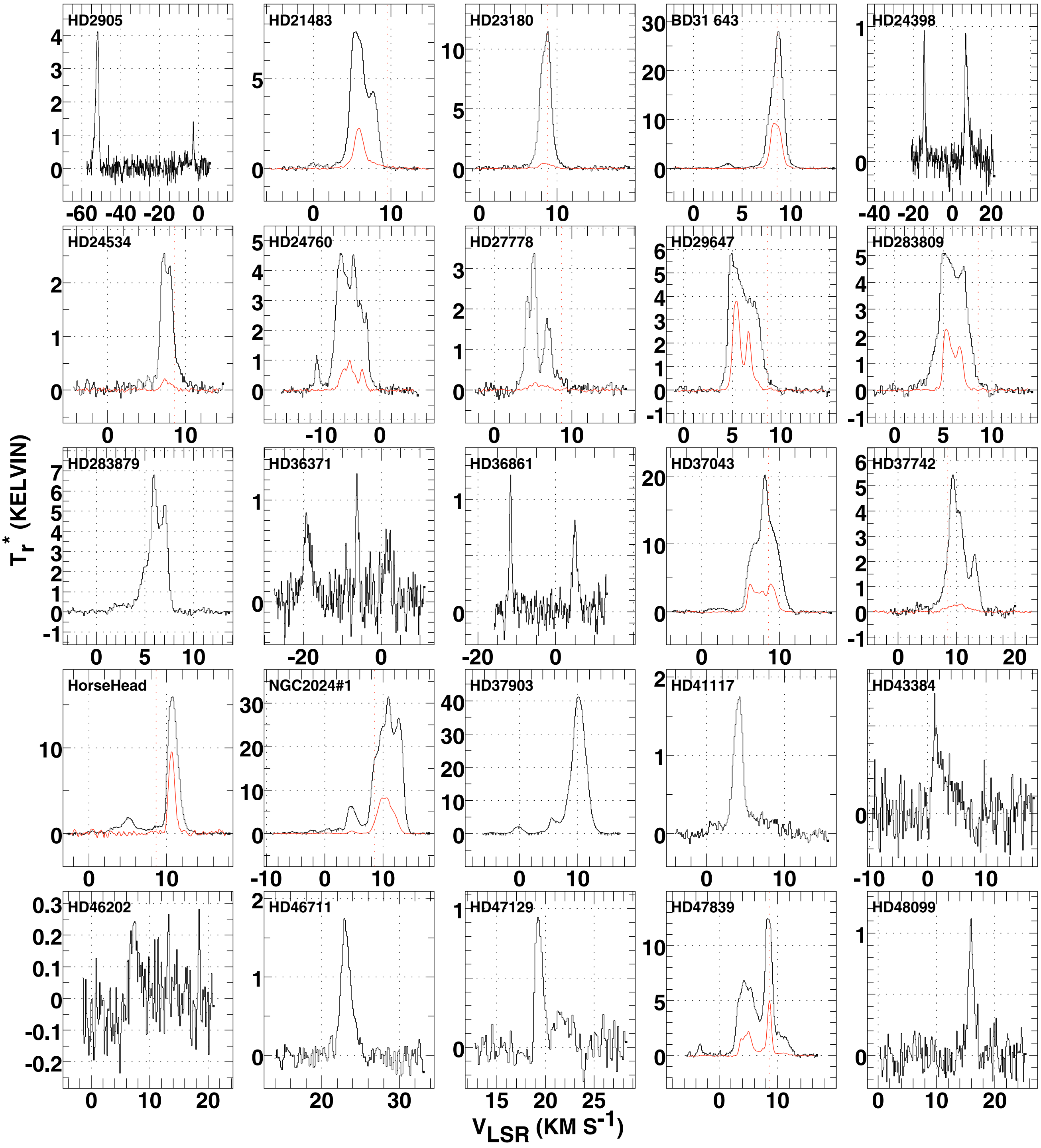

Fig. 1. Observed CO $J = 1–0$ emission profiles. Velocity resolution is generally 0.13 km s^{-1} but a few more extensive profiles have been smoothed to 0.25 km s^{-1}.

for the 71 lines of sight is 0.35 mag corresponding to $A_V \approx 3.1E_{BV} = 1.1$ mag, observing the diffuse cloud regime $A_V \lesssim 1$ mag. Those sightlines showing CO emission have a somewhat larger overall mean foreground reddening, 0.48 vs. 0.21 mag and a much larger mean limiting reddening, 1.87 vs. 0.48 mag. This is a quantitative demonstration of the bias noted earlier whereby associated material preferentially occurs behind early-type target stars whose foreground extinction has been a priori selected to fall in the diffuse cloud regime. Moreover, CO emission is preferentially detected in the more extreme cases.

4.5. Relationships between W_{CO} and E_{BV}^{∞}

The endowments of limiting reddening and CO emission are generally proportional and their ratio, converted to an equivalent column density of H_2 in Table 5 following Savage et al. (1977), is relatively constant. It is also comparable to typical values of the CO-H_2 conversion factor used to convert CO intensity to H_2 column density, 2×10^{20} H_2(K km s^{-1})$^{-1}$, suggesting that the material represented by E_{BV}^{∞} is largely in molecular form for the larger values of E_{BV}^{∞} which dominate the ensemble mean.

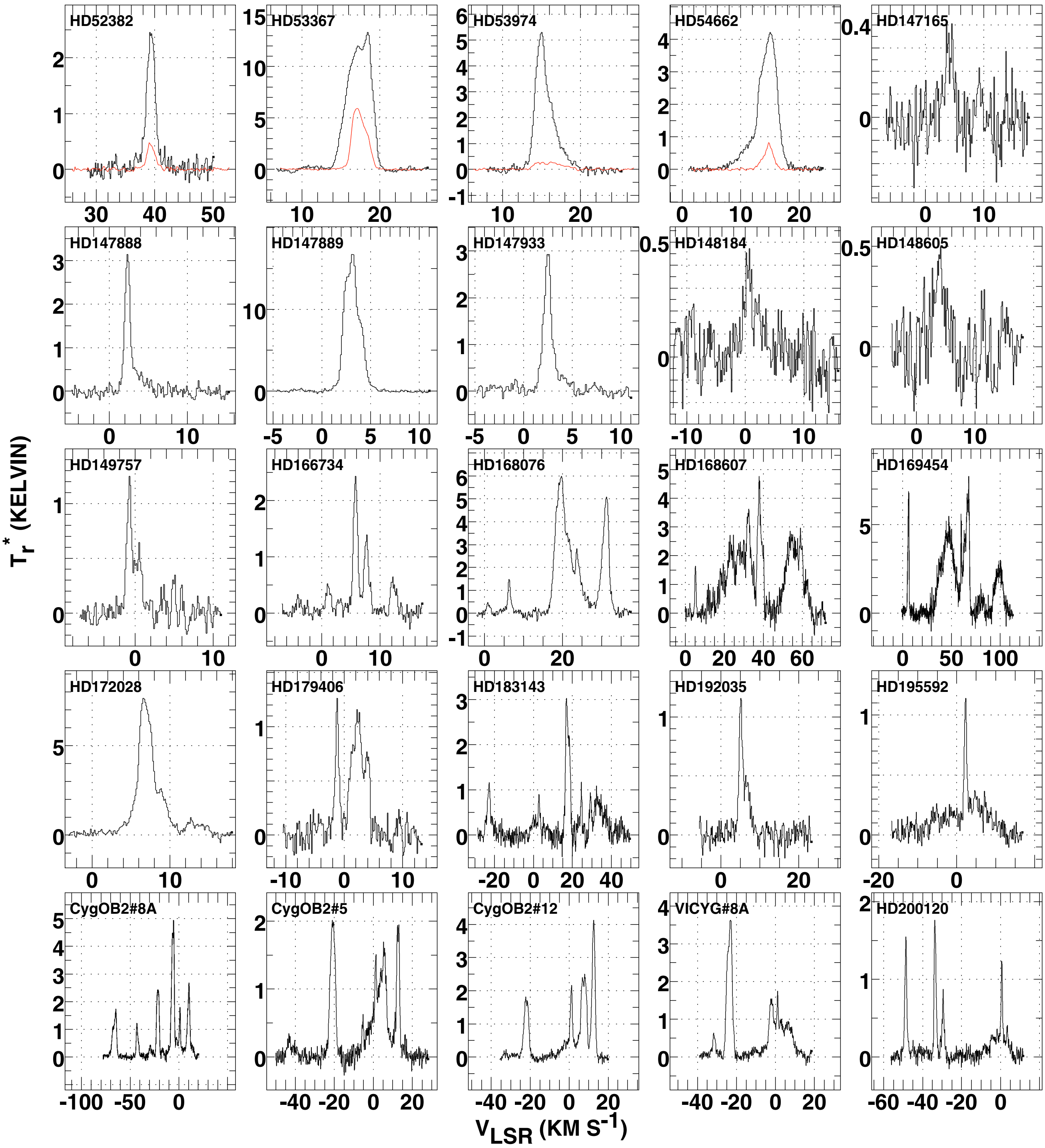

Fig. 2. Observed CO $J = 1$–0 emission profiles, as in Fig. 1.

Line of sight effects are expressed differently in Fig. 4. At top, Fig. 4 plots the distribution of $W_{\rm CO}$ with csc(|b|); as observed in the blind surveys for CO emission toward extragalactic continuum sources (Liszt & Wilson 1993; Liszt 1994), there is no plane-parallel stratification of the CO-emitting medium. Unlike in the blind survey, the reason now is not the galactic structure of the local bubble but rather the association of CO-emitting gas with the target stars.

At bottom in Fig. 4, $W_{\rm CO}$ is plotted against the limiting line of sight reddening out to infinity E_{BV}^{∞} from Schlegel et al. (1998). As suggested by the near constancy of $W_{\rm CO}/E_{BV}^{\infty}$ in Table 5 there is a substantial subset of lines of sight which show a proportionality between $W_{\rm CO}$ and E_{BV}^{∞}.

At higher latitudes where the foreground reddening toward the target stars seldom exceeds 0.35 mag corresponding to the diffuse cloud regime, the present survey seldom finds CO emission except along sightlines at $E_{BV}^{\infty} > 0.5$ mag. This is similar to what occurs along the line of sight toward ζ Oph (HD 149757) where $W_{\rm CO} = 1.7$ K km s^{-1}, $E_{BV} = 0.32$ mag and $E_{BV}^{\infty} = 0.55$ mag, but the inherent liklihood of finding lines of sight with such E_{BV}^{∞} at high latitude is much higher in the survey sample here than for randomly chosen lines of sight.

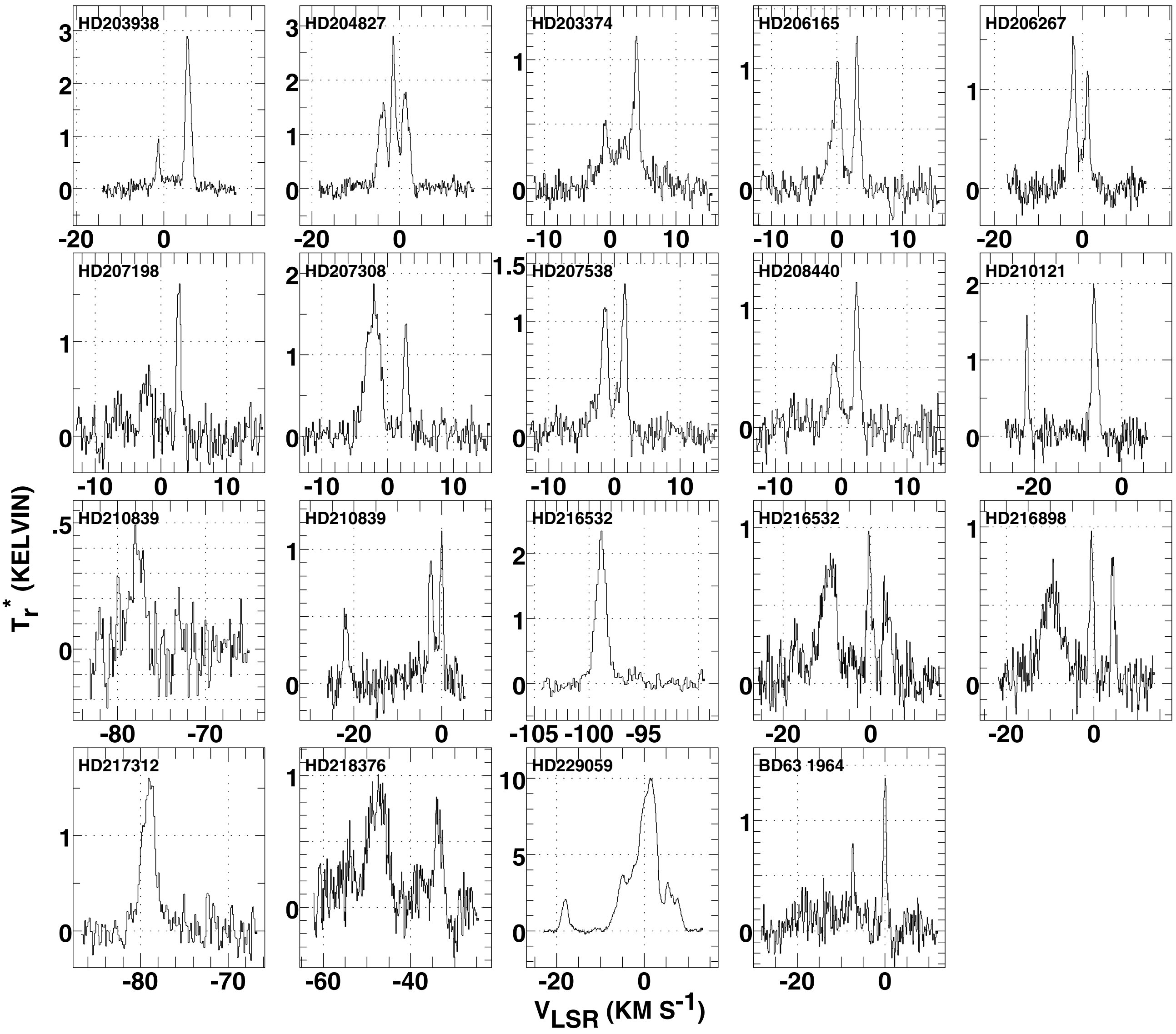

Fig. 3. Observed CO $J = 1$–0 emission profiles, as in Fig. 1.

5. Tracing absorbing gas in emission?

Although it was an original goal of this work to test whether the behaviour predicted for absorbing gas seen in emission could actually be observed, the profound contamination of the survey by background emission from associated material complicates or moots this issue. Given the built-in bias for the target stars to be situated in front of the associated material, the question becomes one of ascertaining whether the emission from foreground absorbing CO may even be reliably identified in arcminute-diameter mm-wave emission fan beams.

The behavior predicted for emission from the foreground absorbing gas takes two forms, as shown in Fig. 6 of Liszt (2007). Most importantly, the integrated intensity should vary as $W_{\rm CO} = \int T_{\rm B} {\rm d}v \approx 1$ K km s^{-1} N(CO)/10^{15} cm^{-2} with no threshold in N(CO) (which varies as $N({\rm H_2})^2$) and little dependence on the ambient number density in the host gas. The proportionality between $W_{\rm CO}$ and N(CO) is a consequence of weak rotational excitation as originally shown by Goldreich & Kwan (1974). This behavior was actually seen in CO emission toward the sample of extragalactic mm-wave background sources where all the gas is in the foreground (Liszt & Lucas 1998).

Figure 5 at bottom shows the comparison between emitted $W_{\rm CO}$ and absorbing N(CO) together with some model results which serve to sketch the expected emission locii for the absorbing gas. CO emission was detected along every line of sight, save one, for which $N({\rm CO}) \gtrsim 4 \times 10^{14}$ cm^{-2}, corresponding approximately to an expected emission contribution $W_{\rm CO} \gtrsim 0.4$ K km s^{-1}. In Sect. 3.2 we estimated a rough a priori 3σ sensitivity limit of 0.22 K, making it appear that CO emission was actually detected to the extent expected, but the emission is contaminated by an uncertain contribution from background gas.

The expectation for the diffuse foreground gas is that the datapoints should lie on or slightly below the model results which are shown (see Fig. 6 of Liszt 2007) and there is a component of the data, about one-third of the detections, for which this is the case. It is these lines of sight for which the contribution from the foreground gas has most likely, not definitely, been isolated. However, many more lines of sight with detected CO are highly overluminous in the ratio $W_{\rm CO}/N$(CO). Given that this ratio is actually maximized in diffuse gas – compare with $W_{\rm CO}/N({\rm CO}) = 500$ K km s^{-1}/3 × 10^{19} cm^{-2} ≈ 15 K km s^{-1}/10^{18} cm^{-2} ≈ 0.02 K km s^{-1}/10^{15} cm^{-2} toward Orion A or a typical dark cloud, respectively – contamination

Table 5. Statistics of E_{BV}, E_{BV}^{∞} and W_{CO}[1].

$\|b\|_<$	N	$E_{BV}^{\infty} > 1$ mag	$\langle E_{BV}^{\infty} \rangle / \langle l \rangle$	CO?	$\langle W_{CO} \rangle / \langle l \rangle$	a $E_{BV}^{\infty}/2W_{CO}$[2]	CO undetected $\langle E_{BV} \rangle$	CO undetected $\langle E_{BV}^{\infty} \rangle$	CO detected $\langle E_{BV} \rangle$	CO detected $\langle E_{BV}^{\infty} \rangle$
	#	#	mag kpc^{-1}	#	K km s^{-1} kpc^{-1}	H cm^{-2} (K km s^{-1})$^{-1}$	mag	mag	mag	mag
3°	71	21	1.4	34	14.1	2.8×10^{20}	0.21	0.48	0.48	1.87
5°	63	16	1.66	29	21.3	2.3×10^{20}	0.19	0.41	0.45	1.98
10°0	49	14	2.4	21	35.7	1.9×10^{20}	0.16	0.38	0.41	2.46
15°	36	11	2.8	16	38.6	2.1×10^{20}	0.13	0.42	0.39	2.76
20°	16	1	1.5	4	30.0	1.5×10^{20}	0.12	0.28	0.46	0.58

[1] For explanation of table entries see Sects. 4.2 and 4.3; [2] $a = 5.8 \times 10^{21}$ H cm^{-2} mag^{-1}.

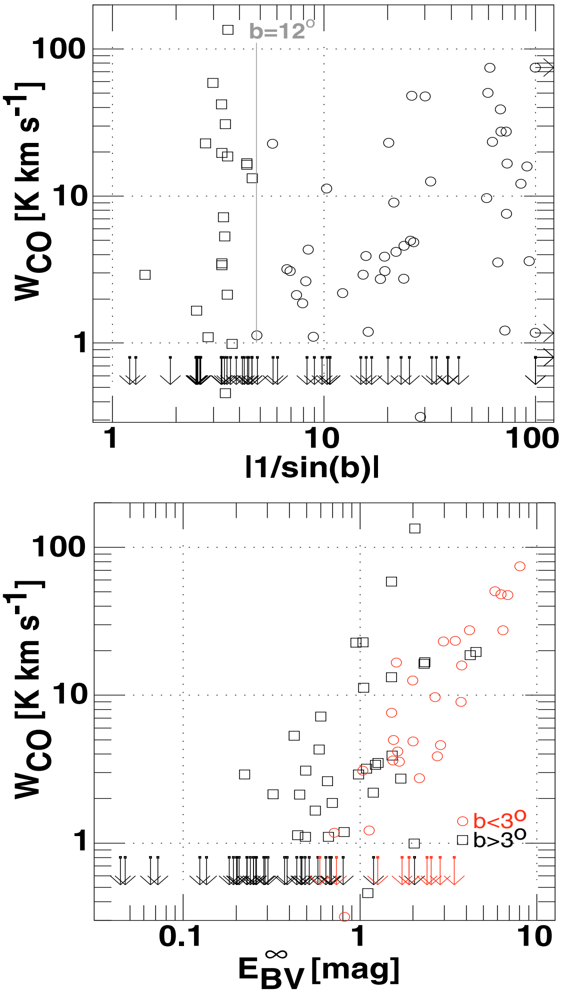

Fig. 4. Variation of the integrated intensity of the CO emission W_{CO}. *Top*: vs. the cosecant of the galactic latitude. *Bottom*: vs. the reddening out to infinity from Schlegel et al. (1998) where lines of sight at lower latitudes are shown as red open diamonds. Lines of sight lacking detectable emission are indicated symbolically.

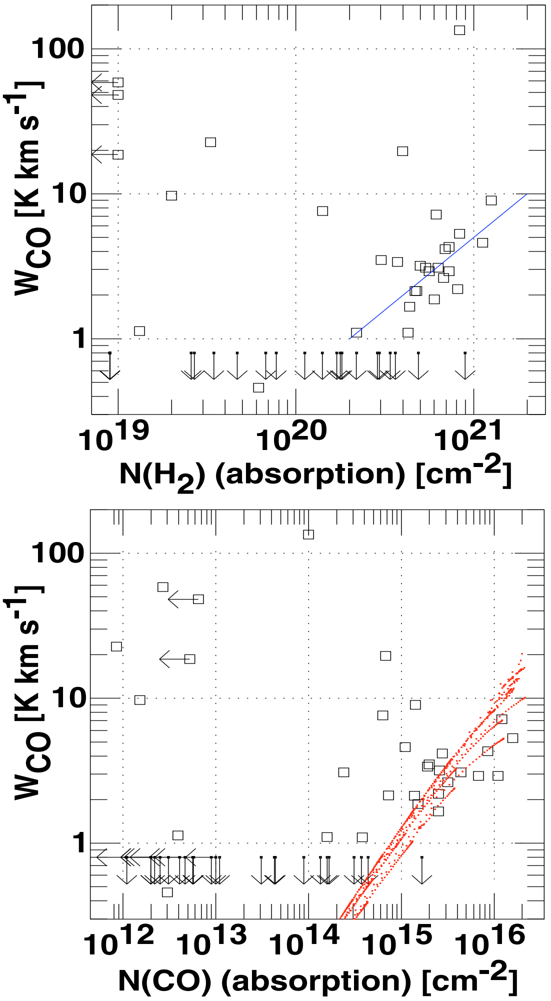

Fig. 5. Variation of the integrated intensity of the CO emission W_{CO}. *Top*: vs. the column density of H_2 seen in absorption. The straight grayed (blue) line represents a CO-H_2 conversion factor $W_{CO}/N(H_2) = 2 \times 10^{20}$ cm^{-2}/(K km s^{-1}). *Bottom*: W_{CO} plotted against the column density of CO seen in absorption. The dotted (red) locii at bottom correspond to the model results for n(H) = 128 and 256 cm^{-3} shown in Fig. 6 of Liszt (2007) and indicate the expected behaviour for foreground gas observed in emission. Lines of sight lacking detectable emission are indicated symbolically.

by background gas is the only possible explanation for such behaviour.

For the absorbing foreground gas, the CO-H_2 conversion factor $W_{CO}/N(H_2)$ should be small for lower $N(H_2)$, only approaching values $W_{CO}/N(H_2) = 1$ K km s^{-1}/2 × 10^{20} cm^{-2} for $N(H_2) \gtrsim 5 \times 10^{20}$ cm^{-2}/(K km s^{-1}). Figure 5 at top shows the observed integrated intensity plotted against the absorbing column density of H_2. The contribution from any underluminous diffuse foreground gas is presumably represented by the non-detections at $N(H_2) \lesssim 5 \times 10^{20}$ cm^{-2} but there is not much of a margin of detectability. What is true is that essentially every line of sight with detected CO emission has $W_{CO}/N(H_2) \gtrsim 1$ K km s^{-1}/1–2 × 10^{20} cm^{-2}. Perversely, most of the very strongest CO emission is found along lines of sight with very small absorbing $N(H_2)$ and N(CO), a sure sign of contamination by background gas.

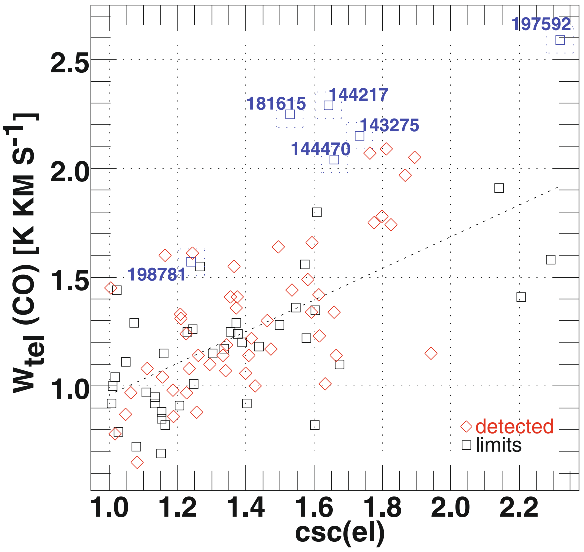

Fig. A.1. Integrated intensity of the telluric CO emission vs. the cosecant of the elevation. Lines of sight with detected and undetected interstellar emission are shown as open rectangles and (red) diamonds, respectively. A few lines of sight from Table 1 without obvious interstellar emission are distinguished by relatively strong telluric emission and are labelled (in blue).

The sole line of sight with appreciable $N(H_2)$ and no CO emission, HD 217035, has $\log N(H_2) = 20.95$ and $\log N(\mathrm{CO}) = 14.57$, a very small fractional CO abundance, and an inferred a foreground emission contribution $W_{\mathrm{CO}} < 0.4$ K km s^{-1}.

6. Summary

To test the predictions made by absorption line observations, and to provide complementary information such as very highly velocity-resolved line profiles, we conducted a survey of the mm-wave $J = 1$–0 ^{12}CO emission toward 110 stars which have in the past served as prime targets for optical/*uv* absorption-line studies of the interstellar molecules H_2, CO, CH, CH$^+$ and $H_3{}^+$. The sample of included sightlines was constructed on the bases of inclusiveness and practicality, i.e. $\delta > -25°$. As discussed in Sect. 3.1, all of the profiles with detected interstellar emission are online in machine readable form along with an additional fourteen profiles of ^{13}CO. Thumbnail sketches of the spectra are shown in Figs. 1–3 and the observations are summarized in Tables 1–4.

The CO emission results were compared with other line of sight parameters such as the total reddening out to infinity, E^{∞}_{BV}, and the absorbing column densities of H_2 and CO, see Sects. 4 and 5. In doing so we showed that the survey sightlines generally are biased toward very high mean density of material (total reddening per unit length typically 2–5 times the local galactic average, see Table 5 and Sect. 4) and comparably large amounts of CO emission .

This can be understood if the targets are physically associated with the neutral material causing the over-density, presumably because they are of early spectral type and were further selected because they returned interesting spectra. In this case the target stars must in general also be interacting with and influencing the associated material, which to this extent can not be entirely typical of the interstellar gas as a whole. The enormous scatter in $N(\mathrm{CO})$ at fixed $N(H_2)$ which is typical of *uv* absorption line surveys may be exaggerated owing to the photoionizing radiation of the target stars. This could also explain why selective photodissociation and fractionation of ^{13}CO are observed in somewhat different degrees in absorption line surveys toward stars and toward extragalactic continuum sources (although small-number statistics may also play a role).

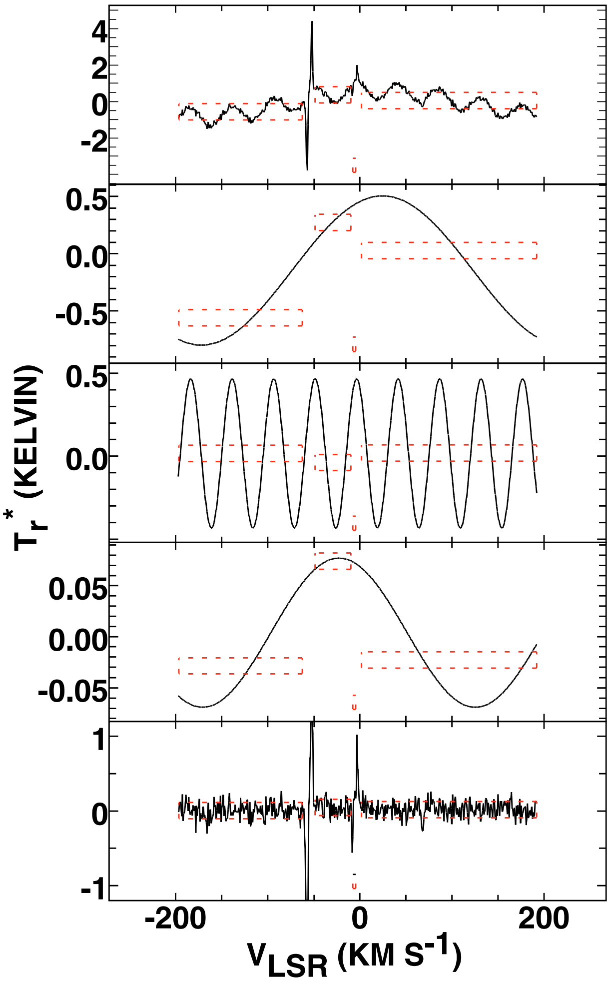

Fig. A.2. Decomposition of an instrumental baseline. *Top*: observed spectrum toward HD 2905, after co-adding both polarizations. *Middle upper to lower*: instrumental sine-wave baselines of period 405, 35.4 and 293 km s^{-1}, found and removed in that order. *Bottom*: spectrum after baseline subtraction. The dashed, inset (red) rectangles show the regions of the spectrum used for baseline detection. The spectra have all been boxcar smoothed over 8 channels for purposes of illustration.

Because the target stars have also been selected to obey the diffuse cloud limit $A_V \lesssim 1$ mag, any overendowment of associated neutral material must occur preferentially behind them. This general scenario is manifested in the detection of some very strong (20–40 K) CO lines typical of natal giant molecular clouds near H II regions, and some heavily saturated lines typical of dark clouds, behind any of which the target stars would not have been suitable candidates for optical/*uv* absorption line studies in the first place. Lines of sight with detectable CO emission are somewhat more highly reddened in the foreground of the target star (0.25 mag) but much more heavily reddened behind (1.5 mag). The effect of association and preferential foreground placement creates complications for observations of CO in emission which lack an innate ability to discriminate between foreground and background material in the vicinity of the star.

Table A.1. Sightlines lacking interstellar CO J = 1–0 emission[1].

Target HD	l °	b °	E_{BV}^{∞} mag	E_{BV} mag	$v_{\rm tel}$ km s^{-1}	rms K	$V_{\rm lsr} - V_{\rm hel}$ km s^{-1}	N(CO) cm^{-2}	N(H$_2$) cm^{-2}
13994	134.39	–3.42	0.64	0.62	–6.17	0.098	3.31		
21856	196.46	–50.96	0.07	0.19	–29.36	0.124	–14.63		20.04
22951	158.92	–16.70	0.46	0.24	–14.08	0.087	–5.96	14.22	20.46
23408	166.17	–23.51	0.69	0.02	–18.11	0.098	–8.66		19.75
23480	166.57	–23.75	0.69	0.08	–17.98	0.169	–8.79		20.12
23630	166.67	–23.46	0.23	0.00	–18.32	0.088	–8.79	<12.34	19.54
23850	167.01	–23.23	0.12	0.01	–18.56	0.162	–8.87		
23840	159.46	–15.03	0.21		–33.41	0.055	–5.94		
24912	160.37	–13.11	0.29	0.33	–12.78	0.066	–6.01	13.49	20.53
30614	144.07	14.04	0.23	0.30	–14.38	0.073	2.51	14.49	20.34
34078	172.08	–2.26	2.40	0.52	–6.72	0.126	–8.21		
35149	199.16	–17.86	0.14	0.11	–14.71	0.107	–16.12	<13.00	18.30
36486	203.86	–17.74	0.24	0.07	–14.17	0.116	–16.93	<12.04	14.74
37128	205.21	–17.24	0.30	0.08	–14.13	0.085	–17.12	<12.30	16.28
42087	187.75	1.77	0.59	0.36	–30.60	0.098	–11.82		
57060	237.82	–5.37	0.52	0.18	–5.79	0.157	–18.84	<12.67	15.78
57061	238.18	–5.54	0.58	0.15	–5.89	0.158	–18.85	<12.61	15.48
58510	235.52	–2.47	0.74		–23.78	0.138	–18.53		
121968	333.97	55.84	0.07	0.07	29.95	0.145	7.56	<12.30	18.70
143275	350.10	22.49	0.25	0.16	18.28	0.099	9.65	12.49	19.41
144217	353.19	23.60	0.27	0.20	35.21	0.116	10.54	13.63	19.83
144470	352.75	22.77	0.39	0.22	34.93	0.120	10.38	12.95	20.05
145502	354.61	22.70	0.49	0.27	34.88	0.120	10.86	12.76	19.89
164353	29.73	12.63	0.20	0.12	10.47	0.086	17.54	13.04	20.26
166937	10.00	–1.60	3.12	0.24	24.39	0.131	12.37		
167971	18.25	1.68	3.42	1.08	5.93	0.129	14.56		
170074	75.06	23.71	0.05		14.80	0.090	18.81		
177989	17.81	–11.88	0.20	0.23	–1.67	0.123	12.41	14.64	20.23
181615	21.84	–13.77	0.18		–2.31	0.153	12.81		
184915	31.77	–13.29	0.26		–2.70	0.101	14.41		20.31
192639	74.90	1.48	1.90	0.66	2.07	0.131	17.46	14.13	20.69
193237	75.83	1.32	1.73	0.63	2.23	0.102	17.34		
197592	30.70	–32.15	0.04		–13.21	0.121	9.93		
198478	85.75	1.49	2.85	0.54	1.09	0.102	16.06		
198781	99.94	12.61	0.47	0.35	6.23	0.066	14.51	15.22	20.56
199579	85.70	–0.30	2.54	0.37	0.23	0.112	15.84		20.36
201345	78.44	–9.54	0.19	0.32	–4.69	0.064	15.41	<12.40	19.43
203064	87.61	–3.84	1.19	0.28	–1.71	0.092	15.03		20.29
206773	99.80	3.62	2.04	0.50	0.55	0.101	13.67	14.20	20.47
209339	104.58	5.87	0.68	0.37	1.96	0.105	12.83	13.95	20.25
209975	104.87	5.39	0.80	0.38	1.80	0.080	12.71		20.08
217035	110.25	2.86	1.18	0.76	–0.26	0.090	11.09	14.57	20.95
217675	102.21	–16.10	0.25	0.05	–10.33	0.135	10.11	12.75	19.67
218915	108.06	–6.89	0.29	0.29	–5.68	0.134	10.30	13.64	20.15
224572	115.55	–6.36	0.38	0.17	–5.99	0.113	8.44		

[1] For explanation of table entries see Sect. 3; all column densities are logarithmic.

One of the original goals of this survey was to compare direct observations with the prediction, based on the observable properties of absorption line gas, that $W_{\rm CO} \approx 1$ K km s^{-1} N(CO)/10^{15} cm^{-2}, with little dependence on the number density of the host gas. The physical origin of such a proportionality resides in very general properties of the weak-excitation limit but the normalization depends on the particular properties of the diffuse gas. For instance, $W_{\rm CO}/N$(CO) is some 50–100 times higher in diffuse gas than when the CO rotation ladder is thermalized, whether in dark clouds ($W_{\rm CO} = 15$ K km s^{-1}, N(CO) = 10^{18} cm^{-2}) or toward Orion A ($W_{\rm CO} = 500$ K km s^{-1}, N(CO) = 3×10^{19} cm^{-2}).

However it seems more likely that the ratio of $W_{\rm CO}$ observed in emission to N(CO) seen in absorption is best used as a gauge of whether the detected emission can reasonably be associated with the foreground absorbing material. Along many lines of sight surveyed here, which have $W_{\rm CO}/N$(CO) much higher than even the already very large value which applies to diffuse gas (see Fig. 5) this is manifestly not so, owing to background contamination. In these cases, the observed CO emission contains

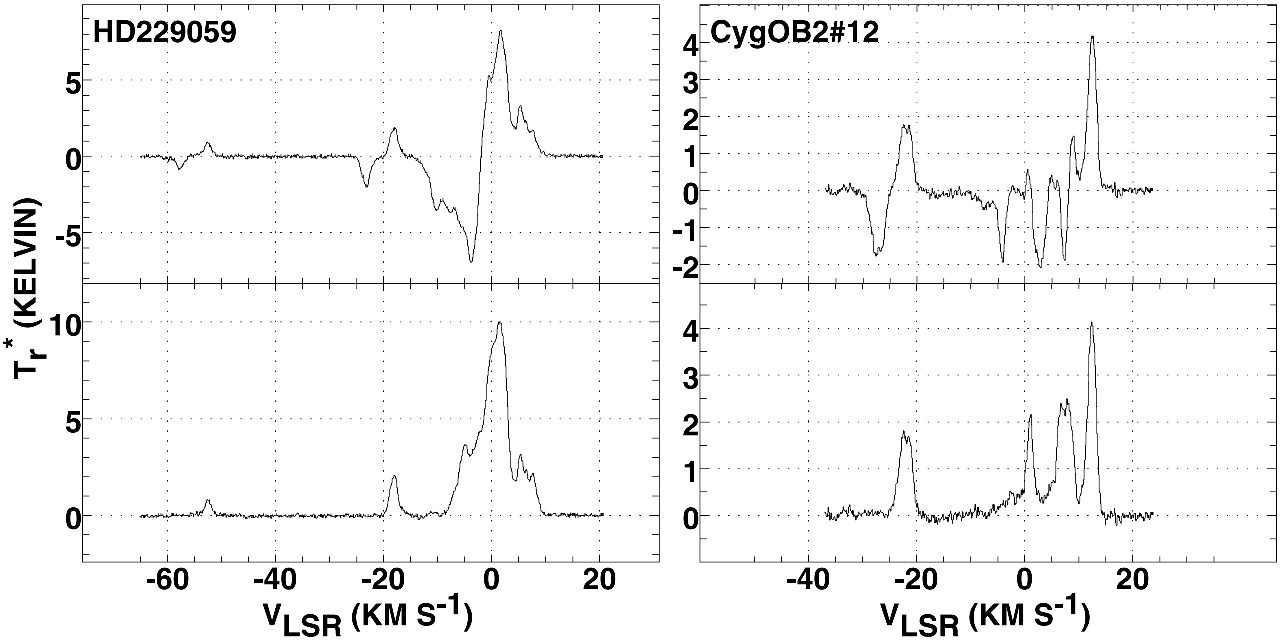

Fig. C.1. Examples of baseline-subtracted frequency-switched (*top*) and unfolded spectra reconstructed with the EKHL algorithm described in Liszt (1997), toward two sources. Compare the spectra at right with Fig. 5 of McCall et al. (2002).

information on the environent of the star, but not necessarily on the foreground gas column. Along other lines of sight, the observed emission may contain a substantial though not necessarily exclusive or even dominant contribution from foreground material.

When the foreground gas can be isolated, CO emission offers the prospect of very highly velocity-resolved line profiles, and, perhaps uniquely, the opportunity to image the host body of the absorbing gas column with high spatial and spectral resolution. These are laudable goals, but, as we have shown here, great care must be exercized in deciding whether they are actually achievable in any individual case. We are currently trying to find sightlines toward bright stars which are good candidates for mapping the foreground gas. In the meantime, a more fruitful approach to mapping diffuse clouds in CO might be to concentrate on those which occult extragalactic background sources, for which confusion between foreground and background material is not an issue.

Appendix A: Telluric emission

A narrow (*FWHM* of 300 kHz or 0.8 km s^{-1}) telluric CO emission line appears with $W_{\rm CO} = 1$–2 K in all frequency-switched spectra. In some spectra, especially at low galactic latitude (for instance toward HD 169454), the telluric emission is inseparable from that originating in the Galaxy. In principle, this could conceal an interstellar line if observations are not made at two epochs widely spaced during the year. In practice the telluric line may appear at velocities which are much larger than those which are likely to appear except at very low galactic latitude.

The velocity at which the telluric line appears in our spectra is given in Tables 1–3 and the measured integral of the telluric emission is shown in Fig. A.1, where lines of sight with and without detected interstellar emission are separately noted. Scatter in the integrated intensity is far larger than that attributable to the typical rms noise level which (see Sect. 2) provides signal/noise levels of about 20:1 with a single channel rms noise level of 0.1 K. The telluric emission fills the entire forward response of the telescope so much of the scatter in Fig. A.1 must be attributed to random errors of calibration. A few lines of sight with non-detections of interstellar emission and exceptionally large telluric CO emission are noted in Fig. A.1. It seems likely that no substantial amount of interstellar emission was missed during the survey.

Note that the present survey includes non-detections in directions where interstellar lines were claimed in the figures of Knapp & Jura (1976), for instance toward P Cyg (HD 193237) and 55 Cyg (HD 198478). In these cases, and for the most negative-velocity component shown by them toward ζ Oph and the highest-velocity components shown toward 9 Cep (HD 206165) and HD 207538, the claimed interstellar line is actually telluric in origin. Other telluric lines are included in their table of claimed detections. This may be verified by noting the dates on which the data of Knapp & Jura (1976) were taken.

Appendix B: Baseline subtraction

Figure A.2 shows the spectrum observed toward HD 2905, along with the three sine-wave components which comprise the spectral baseline. These were detected by least-squares fitting and subtracted in order from uppermost downward. Only the middle component with period near 35 km s^{-1} is capable of concealing a typical isolated interstellar component in spectra away from the galactic equator.

Appendix C: Unfolding

Surveys like that done here are impractical if a clean reference sky position must be found anew for each source (or for too many sources), making use of frequency-switching obligatory. Figure A.3 shows two examples of unfolding frequency-switched spectra using the variant of the EKH dual-beam switching technique (Emerson et al. 1979) described in Liszt (1997) and employed here. The frequency switching interval in both spectra is ±1 MHz, or a total of 5.2 km s^{-1}. In both cases the emission continuously spans substantially more than 5.2 km s^{-1}.

The advantages of this method of observing, which allows faithful reconstruction of signals which are broader than the switching interval, are that it obviates the need for a signal-free off-source reference switching position while permitting narrower frequency switching intervals when searching blindly for the prospective emission profile. Broadening these intervals to avoid switching within a (known or unknown) signal may cause deterioration of the baseline to such an extent that detection of even narrow lines is hindered.

The most obvious disadvantage of the EKHL reconstruction is that the $\sqrt{2}$ gain in signal/noise which accrues to the usual shift and add method of unfolding frequency-switched spectra is not fully realized. Furthermore, unless the spectral baseline can be removed, reconstruction is prone to defects attributable to aliasing.

Because frequency-switching of any kind is a convolution, some spectral components of the signal are unavoidably downweighted corresponding to the smaller Fourier components of the convolution pattern which mathematically represents the shift and subtract process implemented in hardware. With sufficient signal/noise and flat baselines, the EKHL reconstruction will recover all components of the signal which are not entirely filtered out. However, if too much of the sky signal occurs with spectral frequencies which are heavily downweighted during the frequency-switching, reconstruction may be impeded by the actual noise and baseline imperfections. In our experience, such effects are not subtle after reconstruction and the only cure for them is to reobserve with a different frequency switch interval. Only two lines of sight were affected in such a way in this work.

Acknowledgements. The National Radio Astronomy Observatory is operated by Associated Universites, Inc. under a cooperative agreement with the US National Science Foundation. The Kitt Peak 12-m millimetre wave telescope is operated by the Arizona Radio Observatory (ARO), Steward Observatory, University of Arizona. I am grateful to the ARO Director, Dr. Lucy Ziurys for awarding the observing time necessary to perform these observations and to the ARO staff and 12 m operators who keep the telescope running at such a laudably high level. This work profited from many discussions with Jerome Pety and Robert Lucas and remarks by the referee provided an impetus to improve the manuscript.

References

Bally, J., & Langer, W. D. 1982, ApJ, 255, 143
Black, J. H., & Dalgarno, A. 1977, ApJS, 34, 405
Burgh, E. B., France, K., & McCandliss, S. R. 2007, ApJ, 658, 446
Burton, W. B., & Gordon, M. A. 1978, A&A, 63, 7
Crane, P., Lambert, D. L., & Sheffer, Y. 1995, ApJS, 99, 107
Emerson, D. T., Klein, U., & Haslam, C. G. T. 1979, A&A, 76, 92
Federman, S. R., Glassgold, A. E., Jenkins, E. B., & Shaya, E. J. 1980, ApJ, 242, 545
Glassgold, A. E., & Langer, W. D. 1976, ApJ, 206, 85
Glassgold, A. E., Huggins, P. J., & Langer, W. D. 1985, ApJ, 290, 615
Goldreich, P., & Kwan, J. 1974, ApJ, 189, 441
Knapp, G. R., & Jura, M. 1976, ApJ, 209, 782
Langer, W. D., Glassgold, A. E., & Wilson, R. W. 1987, ApJ, 322, 450
Lee, H. H., Herbst, E., Pineau Des Forets, G., Roueff, E., & Le Bourlot, J. 1996, A&A, 311, 690
Liszt, H. 1997, A&AS, 124, 183
Liszt, H. S. 1979, ApJ, 233, L147
Liszt, H. S. 1994, ApJ, 429, 638
Liszt, H. S. 2007, A&A, 476, 291
Liszt, H. S., & Lucas, R. 1998, A&A, 339, 561
Liszt, H. S., & Wilson, R. W. 1993, ApJ, 403, 663
McCall, B. J., Hinkle, K. H., Geballe, T. R., et al. 2002, ApJ, 567, 391
Nehmé, C., Gry, C., Boulanger, F., et al. 2008, A&A, 483, 471
Pety, J., Goicoechea, J. R., Hily-Blant, P., Gerin, M., & Teyssier, D. 2007, A&A, 464, L41
Rachford, B. L., Snow, T. P., Tumlinson, J., et al. 2002, ApJ, 577, 221
Savage, B. D., Drake, J. F., Budich, W., & Bohlin, R. C. 1977, ApJ, 216, 291
Schlegel, D. J., Finkbeiner, D. P., & Davis, M. 1998, ApJ, 500, 525
Sheffer, Y., Rogers, M., Federman, S. R., et al. 2008, ApJ, in press
Sheffer, Y., Rogers, M., Federman, S. R., Lambert, D. L., & Gredel, R. 2007, ApJ, 667, 1002
Smith, A. M., & Stecher, T. P. 1971, ApJ, 164, L43
Sonnentrucker, P., Welty, D. E., Thorburn, J. A., & York, D. G. 2007, ApJS, 168, 58
Spitzer, L. 1978, Physical processes in the interstellar medium (New York: Wiley-Interscience), 333
Stahl, O., Casassus, S., & Wilson, T. 2008, A&A, 477, 865
Van Dishoeck, E. F., & Black, J. H. 1988, ApJ, 334, 771
Wannier, P. G., Penzias, A. A., & Jenkins, E. B. 1982, ApJ, 254, 100
Wilson, R. W., Jefferts, K. B., & Penzias, A. A. 1970, ApJ, 161, L43
Wilson, T. L., Mauersberger, R., Langer, W. D., Glassgold, A. E., & Wilson, R. W. 1992, A&A, 262, 248